Mechanical Systems and Signal Processing 43 (2014) 124–140

Contents lists available at ScienceDirect

Mechanical Systems and Signal Processing

journal homepage: www.elsevier.com/locate/ymssp

Identification of a scaled-model riser dynamics through a combined computer vision and adaptive Kalman filter approach

F.C. Trigo [a,*], F.P.R. Martins [a], A.T. Fleury [a,b], H.C. Silva Jr.[c]

[a] Escola Politécnica da Universidade de São Paulo, Av. Prof. Mello Moraes, 2231, CEP 05508-030 São Paulo, SP, Brazil
[b] Centro Universitário da FEI, Av. Humberto de Alencar Castelo Branco, 3972, CEP 09851-000 São Bernardo do Campo, SP, Brazil
[c] Instituto de Pesquisas Tecnológicas do Estado de São Paulo, Av. Prof. Almeida Prado, 532, CEP 05508-070 São Paulo, SP, Brazil

ARTICLE INFO

Article history:
Received 16 August 2012
Received in revised form
19 September 2013
Accepted 6 October 2013
Available online 25 October 2013

Keywords:
Shaping filter
Non-linear adaptive Kalman filter
Compliant mechanisms
Computer vision
Riser dynamics

ABSTRACT

Aiming at overcoming the difficulties derived from the traditional camera calibration methods to record the underwater environment of a towing tank where experiments of scaled-model risers are carried on, a computer vision method, combining traditional image processing algorithms and a self-calibration technique was implemented. This method was used to identify the coordinates of control-points viewed on a scaled-model riser submitted to a periodic force applied to its fairlead attachment point. To study the observed motion, the riser was represented as a pseudo-rigid body model (PRBM) and the hypotheses of compliant mechanisms theory were assumed in order to cope with its elastic behavior. The derived Lagrangian equations of motion were linearized and expressed as a state-space model in which the state variables include the generalized coordinates and the unknown generalized forces. The state-vector thus assembled is estimated through a Kalman Filter. The estimation procedure allows the determination of both the generalized forces and the tension along the cable, with statistically proven convergence.

1. Introduction

The non-intrusive characteristics of the image-based instrumentation necessary to implement motion analysis is an important advantage of this approach compared to the classical measurement methods based on the use of accelerometers and load cells. Successive advances in the area of computer vision, concerning video segmentation, object tracking and camera calibration, have also contributed to the application of image-based methods to the analysis of kinematics phenomena that are difficult to measure, like the human motion [1], or that occur in regions of difficult access, as the underwater environments [2].

Recently, this technique has been included in the palette of experimental methods of the oceanic and naval engineering center of São **P**aulo **I**nstitute of **T**echnology (IPT, Brazil), in order to improve the quality of the measurements required by the hydrodynamics tests in a towing tank with scaled-models of ships and oceanic structures like platforms and risers (long flexible ducts used by the petroleum industry to pump oil and natural gas to the platforms). Although these measurements have been successfully accomplished with the aid of a motion analysis tool, the camera calibration

* Corresponding author. Tel.: +55 1130915334; fax: +55 1130919642.
E-mail addresses: trigo.flavio@usp.br (F.C. Trigo), flavius.martins@usp.br (F.P.R. Martins), agfleury@fei.edu.br (A.T. Fleury), helio.jr@ipt.br (H.C. Silva Jr.).

0888-3270/$ - see front matter © 2013 Elsevier Ltd. All rights reserved.
http://dx.doi.org/10.1016/j.ymssp.2013.10.005

Nomenclature

PRBM	pseudo-rigid body model
θ_i	PRBM's angular displacements
$\dot{\theta}_i$	PRBM's angular velocities
$\ddot{\theta}_i$	PRBM's angular accelerations
m	PRBM's bar mass
K_i	PRBM's spring coefficients
K_θ	PRBM's standard spring coefficients
L	PRBM's bar lengths
γ	PRBM's largest bar length to actual bar length ratio
p	weight per length ratio
p_s	underwater weight per length ratio
E	modulus of elasticity
I	PRBM's bar section area inertia moment
T	kinetic energy
V	potential energy
L	Lagrangian
$F_{\theta i}$	generalized force at node i
F	traction force

algorithms [3] adopted by this software assume the use of calibration objects to previously measure the three-dimensional space according to a metrological procedure difficult to be done in an underwater environment.

To cope with the various constraints imposed by the measurement environment, several camera self-calibration methods have been proposed in the literature [4–7]. Since these methods are based on invariant geometrical properties of the projective space [8,9], they do not depend on the use of calibration artifacts and, consequently, give rise to a calibrated space that is not limited by the volume of those objects. Such characteristics are especially helpful in the approach of underwater experiments with scaled-model risers.

Although the dynamics of cables has been approached in the early literature of theoretical mechanics [10,11], the recent technological advances observed in the petroleum industry concerning subsea fields extraction has fostered the research of this subject. A thorough investigation about the static and dynamic behaviors of risers under two-dimensional configurations was performed by [12]. Using the theory of thin rods, it was shown that the effect of flexural rigidity is restricted to the regions close to the extremities of the riser; the dynamic model, on the other hand, was formulated as the solution of a perturbation problem around the equilibrium configuration. Both models – the static and the dynamic – were validated against experimental results. Using a finite element program, Campos [13] developed a computational non-linear model for a catenary riser, whose responses, concerning the dynamic bending moments near the touchdown point, are close to the ones derived from the application of previously proposed analytical models. Likewise, in [14], dynamical models through the finite element method representing the catenary riser by beam elements were generated. Firstly, a complete non-linear dynamical model was analyzed using a time-domain technique. Then, the non-linearities of the original model were removed and a frequency-domain technique was applied, giving rise to results that compared well with the previous ones.

Computer vision methods are not yet extensively adopted by the naval laboratories as a measurement tool; therefore, not so many papers have been reported concerning application of those techniques to identify riser kinematics. Bando [15] utilized a single video camera to register the motions of the bottom end of a flexible cable forced to move on a still water test channel through the action of an oscillation mechanism; application of image processing techniques to the successive frames permit to reconstruct the model kinematics and their principal frequencies are finally identified through the use of classical Fourier analysis. Aided by an image processing and computer graphics tool, researchers in [16] constructed a computer vision procedure whose temporal estimates of the scaled model riser configuration were very close to the ones generated by a set of accelerometers fixed to the model. Using classical image segmentation algorithms, in a work by [17], a computer vision procedure was implemented to identify the temporal geometrical variations of a catenary riser near the touchdown point; in his work, the direct linear transformation (DLT) was applied to map the Euclidean three-dimensional space to the projective two-dimensional spaces of the cameras. The DLT was also adopted by [18] to properly calibrate a video camera used to register the motion of small markers distributed on free-vibrating slender columns; moreover, the natural frequencies obtained through modal identification analysis showed excellent agreement with the results anticipated by the theoretical models of slender columns.

Inspection of underground water pipes has also benefited from the use of computer vision techniques for the sake of predictive maintenance, as reported in [19]. In this work, the authors employed a robotic platform on which a laser beam sensor, acting as a range measurement device, performed a two-fold task: first of all, upon scanning the inner surface of pipe, the location of the platform could be determined for positioning control purposes; on the other hand, the scanned profile of the inner pipe, once compared to the a priori known profile, was able to pinpoint anomalies on that surface. An important contribution of this work is the use of a linear Kalman filter to account for uncertainties both on process and on measurement models, which reduced the location error when compared to results obtained directly from the computer vision techniques. Nevertheless, the authors do not state clearly how the covariance matrices, specially the process noise matrix, were tuned. In a laboratory scenario, it does not represent a drawback, since it is always possible to previously scan the basis profile in order to compare with the results coming from processed images; however, in a field environment, one should assure the estimates match the actual profile with statistically proven confidence, which could have been done in this work.

In the present article we use the Lagrangian formalism to construct a simplified lumped dynamic model for a scaled-riser in catenary configuration. Then, the derived motion equations are validated against experimental data using a computer

vision technique to capture the temporal positions of small markers distributed on the riser and a Kalman filter that, using those measurements, estimate the variables that characterize both the kinematics and the dynamics of the riser, as well as an unknown forcing vector which, in analytical mechanics formalism, correspond to a vector of generalized forces. The estimation of this vector is achieved through a shaping filter approach, as detailed in Section 3.1. Convergence of the filter estimates is statistically proven.

2. Materials and methods

2.1. Data acquisition

A scaled-model riser, whose geometrical and physical characteristics are shown in Table 1, was submitted to a series of tests in a towing tank, where the flexible line assumed a typical catenary configuration, with its lower end anchored at the towing tank floor and its fairlead attachment point hinged to a harmonic oscillator assembled on a platform over the water line (Fig. 1a and b). The riser motion is known from the time evolution of the locations of 200 mm equally spaced small circular markers attached to the line, and is recorded by a high resolution video camera (JAI CV-A1) coupled to a varifocal lens (6–12 mm). Connected to an asynchronous frame grabber (Coreco-Imaging PC2-Vision) and inserted on a water-proof canister installed inside the tank, the image acquisition system was set up to record up to 4 MB monochromatic images of the region near the touchdown zone at the frequency of 100 MB/s.

Using the above referred image acquisition system, a series of images describing the planar motion of the scaled model riser were collected.

Considering that the riser segment near the touchdown point remains parallel to the horizontal line (see Fig. 1), the images generated by the experimental setup easily permit to estimate the inclination angle α between the image horizontal axis and the image towing bottom line (see Fig. 2a). Furthermore, the measurement of distances between successive markers in the rotated image of Fig. 2b along its horizontal axis indicate that the horizontal scale does not change with position, i.e.,

$$d_{1,2} = d_{2,3} = \ldots d_{n-1,n} = d \tag{1}$$

Table 1
Characteristics of the scaled-model riser.

Characteristics	Value
Length (m)	8.190
Diameter (m)	0.254
Flexural rigidity (kg m^2)	1.337×10^{-6}
Linear density (kg/m)	0.2190
Submerged linear density (kg/m)	0.1001

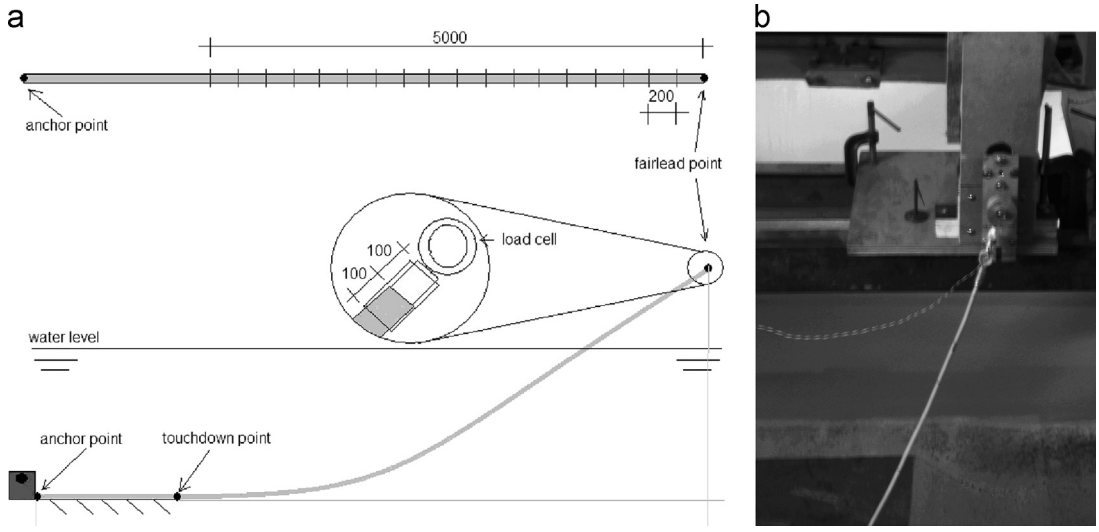

Fig. 1. (a) Schema of the experimental setup; (b) detail of the fairlead point.

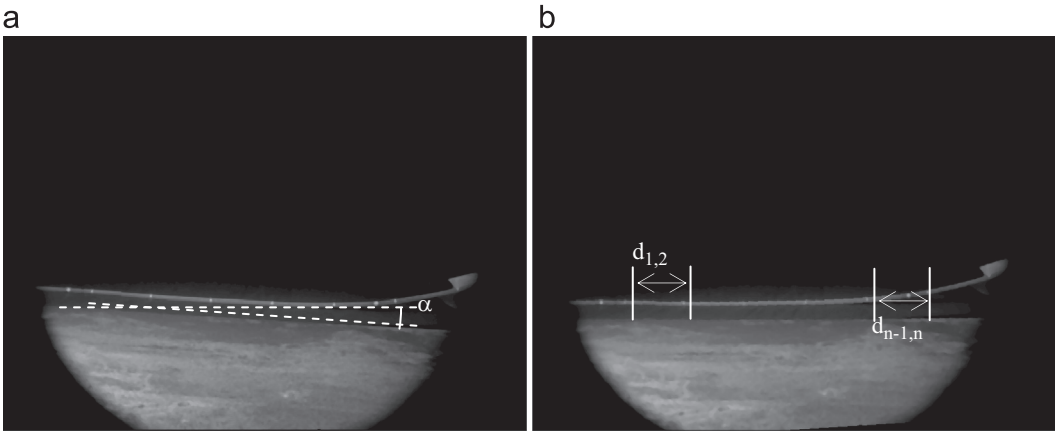

Fig. 2. (a) Original image. (b) Image (a) rotated in order to align the towing bottom line with the horizontal axis.

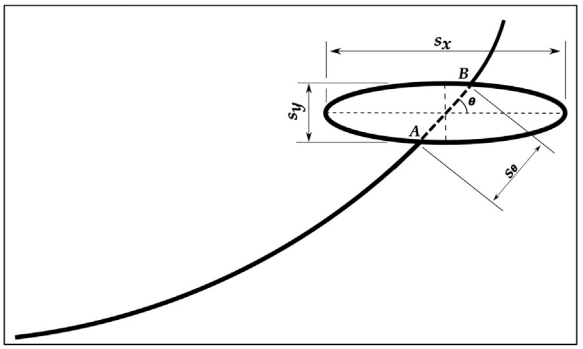

Fig. 3. Measurement of the scale factors along a generic direction of the image plane.

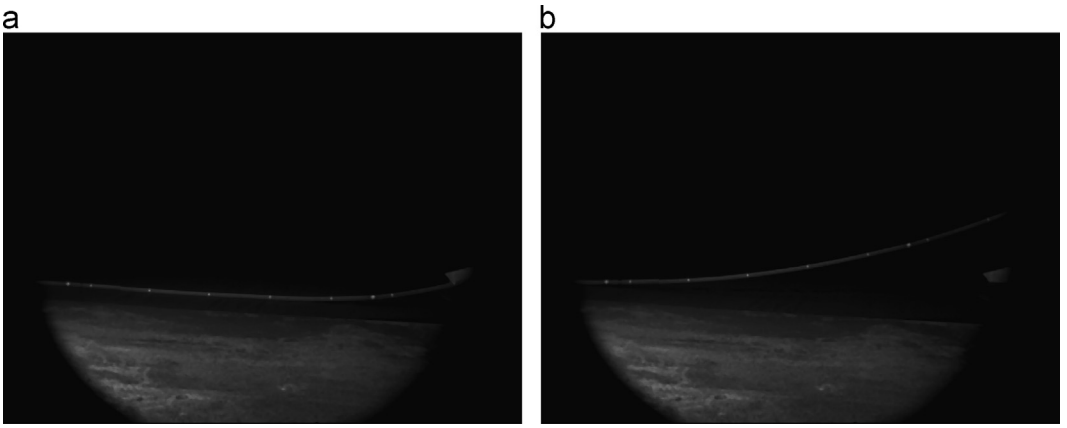

Fig. 4. (a) Reference image I_{ref}: model riser at its lowest position; (b) image $I(t)$: model riser at instant t.

The above results permit us to assume that the projective transformation applied by the camera can be approximated by an affinity [8] (see Fig. 3) with uniform horizontal and vertical scales estimated, respectively, by

$$s_x = \frac{\ell}{d} \tag{2}$$

$$s_y^2 = \frac{(s_\theta s_x \sin\theta)^2}{s_x^2 - s_\theta^2 \cos^2\theta} \tag{3}$$

where l, the distance between markers, is a priori known (200 mm), θ is the angle between the segment AB and the horizontal line and s_θ is the scale measured along the segment AB.

2.2. Image preprocessing

All the images were submitted to a segmentation process encompassing three steps: (1) background removal; (2) image segmentation; (3) determination of the centroids of the markers.

Using a pair of images I_{ref} and $I(t)$, where the first (Fig. 4a), named 'reference image', corresponds to a configuration where the riser is at its lowest position and the second (Fig. 4b) is an image grabbed at instant t, the process of background removal can be accomplished through the following computer vision algorithm:

a. $I_1 = I(t) - I_{ref}$
b. $I_2(x,y) = \ln(1 + I_1(x,y))$
c. $I_3(x,y) = \begin{cases} 255 & \text{if } I_2(x,y) > t_{opt}, \text{ where } t_{opt} \text{ is the optimal threshold} \\ 0 & \text{otherwise} \end{cases}$
d. $I_4 = I_3 \circ Circ\,(R=4)$
e. $I_5 = I_4 \oplus Circ\,(R=1)|_{I_3}$
f. $I_6(x,y) = \min\{I_1(x,y), I_5(x,y)\}$

The image subtraction operation of step (a) above preserves the object of interest (i.e., the riser) at instant t but does not completely eliminate the image background. The application of a logarithmic look-up table at the difference image I_2

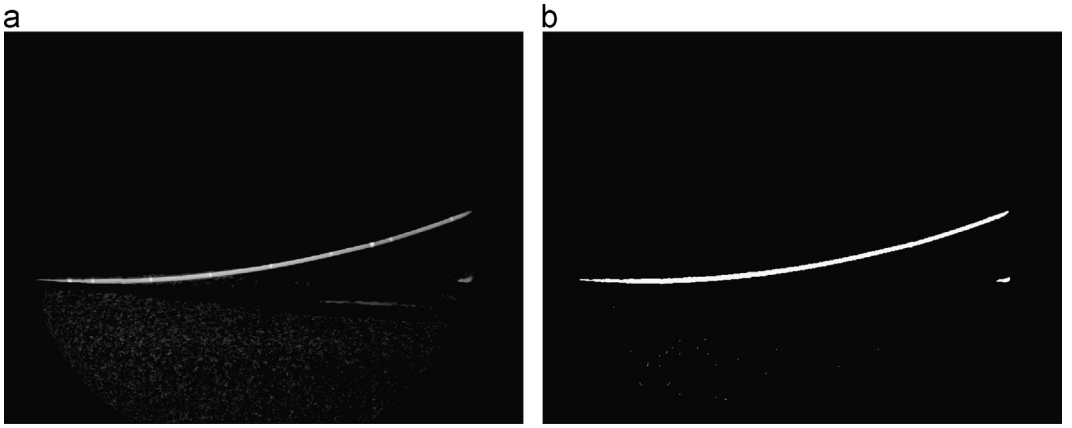

Fig. 5. (a) I_2: image difference $I(t) - I_{ref}$ (Fig. 4a and b) enhanced through the application of a logarithmic lookup table; (b) I_3: image I_2 thresholded according to Otsu's algorithm.

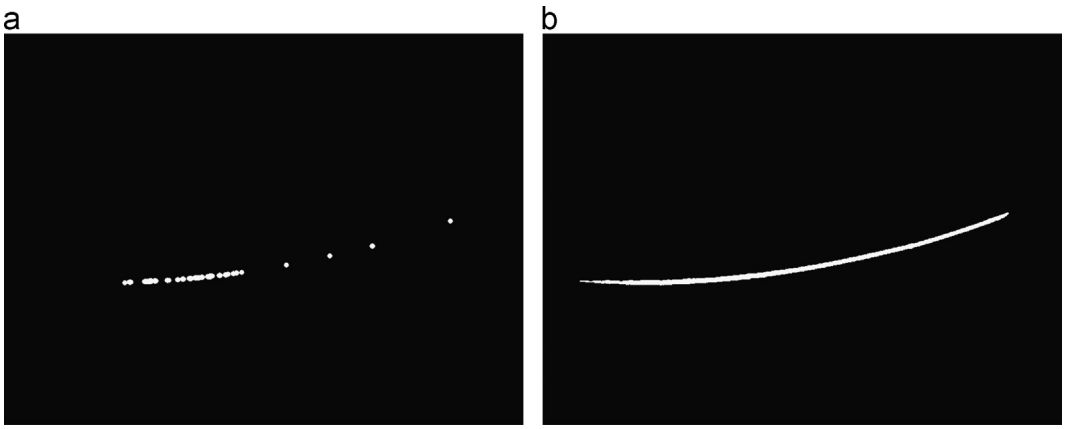

Fig. 6. (a) I_4: image I_3 (shown in Fig. 5b) opened by a structuring element 'circle' of radius 1 pixel; (b) image I_5: geodesic dilation of the image I_4 using image I_3 as the reference image.

enhances its gray levels permitting that the optimal thresholding operation based on Otsu's algorithm [20] generate, at the end of step (c), an image I_3 where one of the binary objects completely contains the riser (Fig. 5). Applying on I_3 an opening operation [21] with a structure element 'circle' of radius $R=1$ pixel, followed by a geodesical dilation of the last image using I_3 as the reference image, generate a proper mask to select in the difference image I_1 only the pixels around the riser (Fig. 6). Finally, the object of interest emerges after applying a minimum operation based on the mask I_5 and the difference image I_1 (Fig. 7).

The segmentation process is based upon the following computer vision algorithm:

a. $I_7 = grad(I_6)$

b. $I_8(x,y) = \begin{cases} 255 & \text{if } I_7(x,y) > 60 \\ 0 & \text{otherwise} \end{cases}$

c. $I_9 = I_8 \circ Circle\ (R=1)$

In order to enhance the targets of image I_6, the Sobel edge detector [23] is applied to it (Fig. 8a). Then, by thresholding the resultant image at a fixed gray level and opening it by a structuring element 'circle' of radius $R=1$ pixel, an image (I_9) exhibiting only isolated objects around the targets emerges (Fig. 8b).

To identify the centroid of the targets, the following computer vision algorithm is adopted:

a. $I_{10} = Skeleton(I_9)$
b. $I_{11} = Hitmiss\ (I_{10},\ Golay\ Element\ (Bifurcation\ pixels))$
c. $I_{12} = Hitmiss\ (I_{10},\ Golay\ Element\ (Extreme\ pixels))$

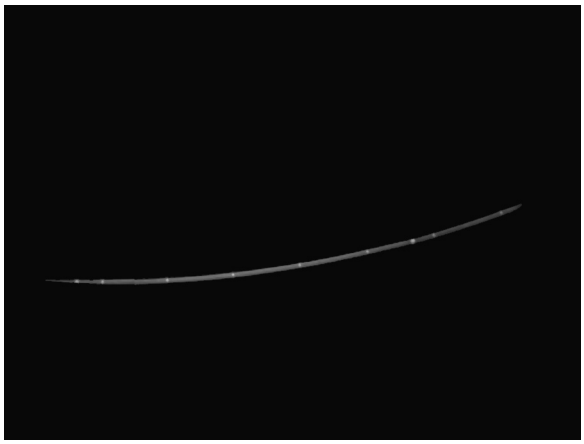

Fig. 7. I_6: riser image after the application of the background removal algorithm.

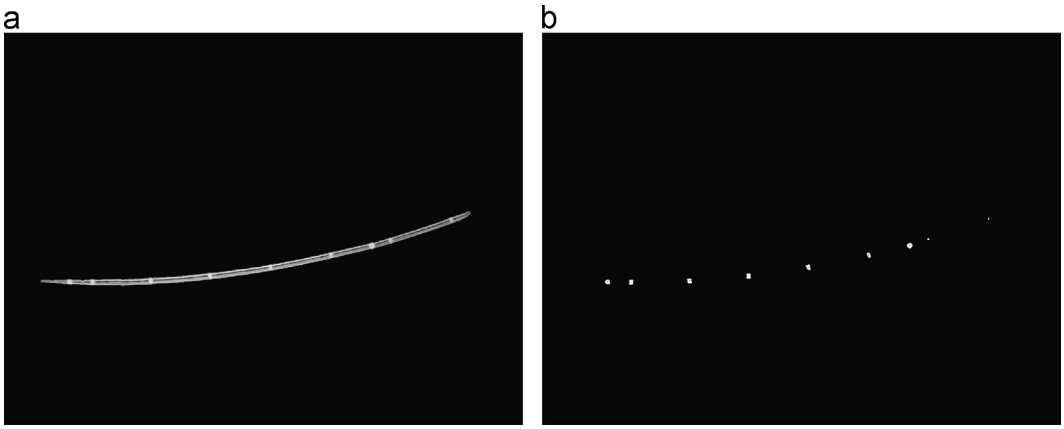

Fig. 8. (a) I_7: gradient of image I_6 (shown in Fig. 7) exhibited in a logarithmic gray scale; (b) I_9: image I_7 after being thresholded and opened by a structuring element 'circle' of radius 1 pixel.

Fig. 9. Image I_{10}: morphological skeleton of the image I_9 (shown in Fig.8b).

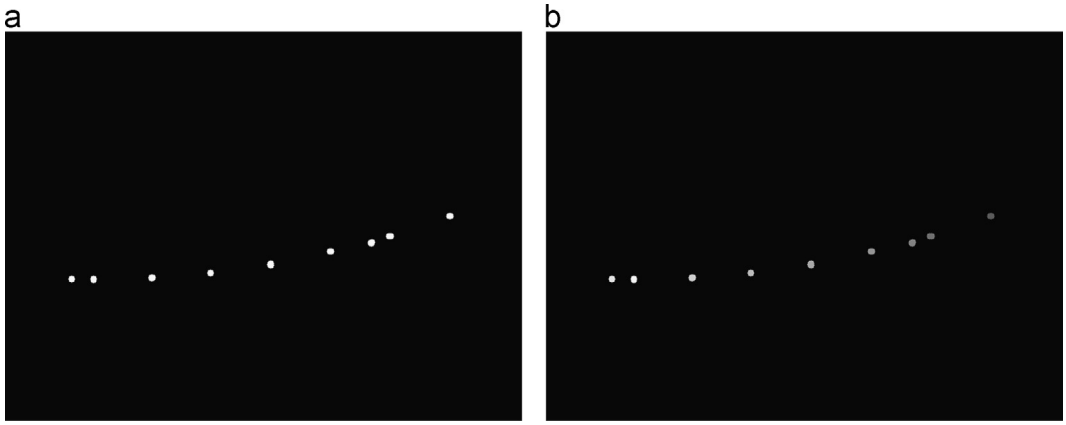

Fig. 10. (a) I_{17}: image of centered isolated objects around the targets; (b) labeled image: each target is pictured with a given gray level.

d. $I_{13} = I_{11} \oplus Circle\ (R=5)$
e. $I_{14} = I_{12} \oplus Circle\ (R=5)$
f. $I_{15} = I_{13} \oplus Circle\ (R=1)|_{I_{12}}$
g. $I_{16}(x,y) = \min\{I_{13}(x,y), I_{14}(x,y)\}$
h. $I_{17}(x,y) = \max\{I_{15}(x,y), I_{12}(x,y)\}$
i. $objects = labelling\_image\ (I_{17})$

Application of a skeletonization operation based on the '*L*' Golay element [22] gives rise to an image (Fig. 9) where both bifurcation and extreme points can be easily isolated through the above hit-miss morphological operations (b) and (c), using proper Golay's elements.

Operations (d)–(h) above, aimed at producing objects nearly centered to the medial axis of images I_{11} and I_{12}, give rise to image I_{17} (Fig. 10a). Applying to this image a classic labeling algorithm [23], the centroid coordinates of each marker (Fig. 10b) can be easily calculated.

After applying to the rotated images a segmentation process featured to isolate the image centroids (xim_i,yim_i) of the markers, their motion plane coordinates (x_i,y_i) were obtained by a simple scaling operation. So, observations of the scaled model riser kinematics could be properly described along the time.

3. Theoretical background

3.1. Riser dynamic model

Using the theory of compliant mechanisms [24], the scaled-model riser was represented as a pseudo rigid body model (PRBM) composed of segments of rigid bars linked by torsional springs (see Fig. 11) with constants that depend on the respective boundary conditions. As illustrated in Fig. 11, the number of degrees of freedom of the generated model is compatible with the observed kinematics data and the PRBM's equivalent compliant properties of the mechanism are calculated according to the expressions suggested by [25] concerning flexible beams submitted to some previously established load and boundary conditions.

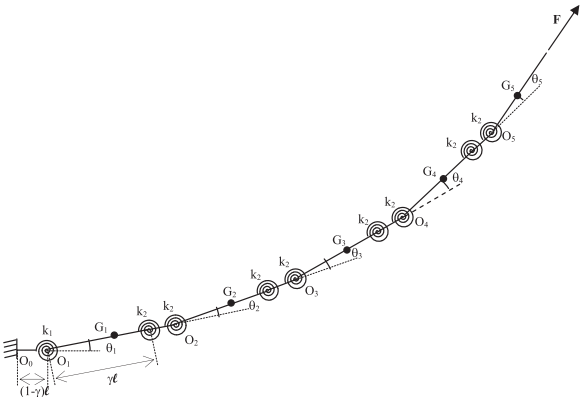

Fig. 11. PRBM for the-scaled model riser.

For a fixed–fixed beam boundary condition, the spring constant is

$$K=\frac{2\gamma K_\theta EI}{\ell} \tag{4}$$

where, according to [24], $\gamma=0.85$ and $K_\theta=2.6$.

Considering that all the springs or pairs of springs correspond to the same fixed–fixed beam boundary conditions, then

$$k_1=k_2=K=\frac{2\gamma K_\theta EI}{\ell} \tag{5}$$

Moreover, the serial pairs of springs can be substituted by an equivalent spring with constant given by

$$k'_2=\frac{k_2}{2}=\frac{\gamma K_\theta EI}{\ell} \tag{6}$$

In order to write the Lagrangian equations for the compliant mechanism of Fig. 11, the expressions for the kinetic energy, the potential energy and the generalized forces were properly developed.

The kinetic energy is given by

$$T=\frac{1}{2}\sum m_i v_{Gi}^2+\frac{1}{2}\sum J_{Gi}\dot{\theta}_i^2,\quad i=1,\ldots,5 \tag{7}$$

where

$$\vec{v}_{Gi}=\vec{v}_{Oi}+\dot{\theta}\vec{k}\wedge(G_i-O_i),\quad i=1,\ldots,5 \tag{8}$$

and J_{Gi} is the moment of inertia of the segment $O_{i-1}O_i$.

After substituting (8) in (7), the following expression for the kinetic energy results:

$$\begin{aligned}T=&\frac{m\ell^2}{2}\left[\left(\frac{\gamma^2}{4}+4\right)\dot{\theta}_1^2+\left(\frac{\gamma^2}{4}+3\right)\dot{\theta}_2^2+\left(\frac{\gamma^2}{4}+2\right)\dot{\theta}_3^2+\left(\frac{\gamma^2}{4}+1\right)\dot{\theta}_4^2+\frac{\gamma^2}{4}\dot{\theta}_5^2\right]\\&+\frac{m\ell^2}{2}\left[(6+\gamma)\dot{\theta}_1\dot{\theta}_2\cos\theta_2+(4+\gamma)\dot{\theta}_1\dot{\theta}_3\cos(\theta_2+\theta_3)+(2+\gamma)\dot{\theta}_1\dot{\theta}_4\cos(\theta_2+\theta_3+\theta_4)\right]\\&+\frac{m\ell^2}{2}\left[\gamma\dot{\theta}_1\dot{\theta}_5\cos(\theta_2+\theta_3+\theta_4+\theta_5)\right]\\&+\frac{m\ell^2}{2}\left[(4+\gamma)\dot{\theta}_2\dot{\theta}_3\cos\theta_3+(2+\gamma)\dot{\theta}_2\dot{\theta}_4\cos(\theta_3+\theta_4)+\gamma\dot{\theta}_2\dot{\theta}_5\cos(\theta_3+\theta_4+\theta_5)\right]\\&+\frac{m\ell^2}{2}\left[(2+\gamma)\dot{\theta}_3\dot{\theta}_4\cos\theta_4+\gamma\dot{\theta}_3\dot{\theta}_5\cos(\theta_4+\theta_5)+\gamma\dot{\theta}_4\dot{\theta}_5\cos\theta_5\right]\\&+\frac{J}{2}\left[\dot{\theta}_1^2+(\dot{\theta}_1+\dot{\theta}_2)^2+(\dot{\theta}_1+\dot{\theta}_2+\dot{\theta}_3)^2+(\dot{\theta}_1+\dot{\theta}_2+\dot{\theta}_3+\dot{\theta}_4)^2+(\dot{\theta}_1+\dot{\theta}_2+\dot{\theta}_3+\dot{\theta}_4+\dot{\theta}_5)^2\right]\end{aligned} \tag{9}$$

The potential energy of the scaled-model riser encompasses the energy stored in the springs and the potential of the gravitational and hydrostatic forces. So, it is described by

$$\begin{aligned}V=&\frac{1}{2}(k_1\theta_1^2+k_2\theta_2^2+k_2\theta_3^2+k_2\theta_4^2+k_2\theta_5^2)\\&+p_s\ell^2\left[\left(4+\frac{\gamma}{2}\right)\sin\theta_1+\left(3+\frac{\gamma}{2}\right)\sin(\theta_1+\theta_2)+\left(2+\frac{\gamma}{2}\right)\sin(\theta_1+\theta_2+\theta_3)\right]\end{aligned}$$

$$+p_s\ell^2\left[\left(1+\frac{\gamma}{2}\right)\sin(\theta_1+\theta_2+\theta_3+\theta_4)+\left(1+\frac{\gamma}{2}\right)\sin(\theta_1+\theta_2+\theta_3+\theta_4+\theta_5)\right] \tag{10}$$

where p_s is the underwater weight per length ratio.

The generalized force $F_{\theta i}$ (physically, a bending moment) applied at the node O_5, is

$$F_{\theta i}=F_x\frac{\partial x_5}{\partial\theta i}+F_y\frac{\partial y_5}{\partial\theta i} \tag{11}$$

adopting $L=T-V$ and applying to Eqs. (9)–(11) above the Lagrangian equations, given by

$$\frac{d}{dt}\left(\frac{\partial L}{\partial\dot{\theta}_i}\right)+\left(\frac{\partial L}{\partial\theta_i}\right)=F_{\theta i} \tag{12}$$

it is generated the complete set of nonlinear dynamics equations that govern the motion of the discretized multibody system representing the scaled-model riser. Those equations are shown in Appendix A.

After linearizing Eqs. (A-1)–(A-5), we obtain

$$\left[\tfrac{m\ell^2}{2}\left(\tfrac{\gamma^2}{2}+4\right)+5J\right]\ddot{\theta}_1+\left[\tfrac{m\ell^2}{2}(6+\gamma)+4J\right]\ddot{\theta}_2+\left[\tfrac{m\ell^2}{2}(4+\gamma)+3J\right]\ddot{\theta}_3+\left[\tfrac{m\ell^2}{2}(2+\gamma)+2J\right]\ddot{\theta}_4+\left[\tfrac{m\ell^2}{2}\gamma+J\right]\ddot{\theta}_5$$
$$+k_1\theta_1+p_s\ell^2\left(10+\frac{5}{2}\gamma\right)=F\ell(\theta_2+2\theta_3+3\theta_4+4\theta_5) \tag{13}$$

$$\left[\tfrac{m\ell^2}{2}(6+\gamma)+4J\right]\ddot{\theta}_1+\left[m\ell^2\left(\tfrac{\gamma^2}{4}+3\right)+4J\right]\ddot{\theta}_2+\left[\tfrac{m\ell^2}{2}(4+\gamma)+3J\right]\ddot{\theta}_3+\left[\tfrac{m\ell^2}{2}(2+\gamma)+2J\right]\ddot{\theta}_4+\left[\tfrac{m\ell^2}{2}\gamma+J\right]\ddot{\theta}_5$$
$$+k_2\theta_2+p_s\ell^2(6+2\gamma)=F\ell(\theta_3+2\theta_4+3\theta_5) \tag{14}$$

$$\left[\tfrac{m\ell^2}{2}(4+\gamma)+3J\right]\ddot{\theta}_1+\left[\tfrac{m\ell^2}{2}(4+\gamma)+3J\right]\ddot{\theta}_2+\left[m\ell^2\left(\tfrac{\gamma^2}{4}+2\right)+3J\right]\ddot{\theta}_3+\left[\tfrac{m\ell^2}{2}(2+\gamma)+2J\right]\ddot{\theta}_4+\left[\tfrac{m\ell^2}{2}\gamma+J\right]\ddot{\theta}_5$$
$$+k_2\theta_3+p_s\ell^2\left(3+\frac{3}{2}\gamma\right)=F\ell(\theta_4+2\theta_5) \tag{15}$$

$$\left[\tfrac{m\ell^2}{2}(2+\gamma)+2J\right]\ddot{\theta}_1+\left[\tfrac{m\ell^2}{2}(2+\gamma)+2J\right]\ddot{\theta}_2+\left[\tfrac{m\ell^2}{2}(2+\gamma)+2J\right]\ddot{\theta}_3+\left[m\ell^2\left(\tfrac{\gamma^2}{4}+1\right)+2J\right]\ddot{\theta}_4+\left[\tfrac{m\ell^2}{2}\gamma+J\right]\ddot{\theta}_5$$
$$+k_2\theta_4+p_s\ell^2(1+\gamma)=F\ell\theta_5 \tag{16}$$

$$\left[\frac{m\ell^2}{2}\gamma+J\right]\ddot{\theta}_1+\left[\frac{m\ell^2}{2}\gamma+J\right]\ddot{\theta}_2+\left[\frac{m\ell^2}{2}\gamma+J\right]\ddot{\theta}_3+\left[\frac{m\ell^2}{2}\gamma+J\right]\ddot{\theta}_4+\left[\frac{m\ell^2\gamma^2}{2\ \ 2}+J\right]\ddot{\theta}_5+k_2\theta_5+p_s\ell\frac{\gamma}{2}=0 \tag{17}$$

3.2. Estimation of displacements and forces

The set of linearized differential Eqs. (13)–(17) in the generalized coordinates must now be solved for those coordinates and for the unknown cable tension F. This forcing term acts directly only at the free-end of the outermost right bar segment. However, its effect at the right edges of the four remaining bar segments of the compliant mechanism model is accounted for as equivalent generalized forces (physically, bending moments obtained when the cable tension is transferred from point G_5 (see Fig. 11) to the other segment edges); for this reason, tension F appears as a common factor at the right side of Eqs. (13)–(16).

In order to solve the stated problem, we formulate it as a state-space problem and use a Kalman filter to estimate the state, a vector containing the generalized coordinates, their derivatives plus the non-modeled forcing terms. The approach we used to obtain the state-space model is described next.

Eqs. (13)–(17) describe a continuous time lumped-parameter model approach to the suspended cable problem; in matrix notation, they can be written as

$$[M]\ddot{\underline{\theta}}(t)+[K]\underline{\theta}(t)=\underline{\Psi}(\underline{\theta}(t),F), \tag{18}$$

in which $[M]$, $[K]\in R^{5x5}$ are respectively the inertia and stiffness matrices, $\underline{\theta}(t)\in R^{5x1}$ is a vector of generalized coordinates and $\underline{\Psi}\in R^{5x1}$ accounts for all terms that contain bi-linear functions of the generalized coordinates and of the unknown cable tension, plus independent constant terms that come from field energies. Damping is not included in this model because a simplified approach was adopted; however, we intend to include the estimation of a damping matrix in future works. As it is noticeable from Eqs. (13) to (17), the continuous-time model thus assembled is coupled in the second derivatives, i.e., matrix $[M]$ is not diagonal; however, since it is real and symmetric, it is always possible to write a linear map $L:\ \underline{\theta}\rightarrow\underline{\eta}$ such that

$$\underline{\theta}(t)=[L]\underline{\eta}(t), \tag{19}$$

with $[L]$ a square non-singular constant matrix or order 5. As a consequence of substitution of Eq. (19) into Eq. (18) and multiplication of both sides by $[L]^T$, one obtains

$$[L]^T[M][L]\ddot{\underline{\eta}}(t)+[L]^T[K][L]\underline{\eta}(t)=[L]^T\underline{\Psi}(\underline{\theta}(t),F), \tag{20}$$

or, in shorter form,

$$[M_d]\ddot{\underline{\eta}}(t)+[K_s]\underline{\eta}(t)=\underline{\Omega}(\underline{\theta}(t),F), \tag{21}$$

with $[M_d]$ a diagonal matrix and $[K_s]$ a symmetric matrix, thus decoupling the system in the second derivatives of the generalized coordinates and allowing its description in a canonical state-space framework. In this work, we employed an appropriate built-in function of the open-source software *Octave* to obtain the transformation matrix $[L]$. The components of the state-vector are, then, $x_i(t)$, $i=1:10$ with

$$\begin{array}{llll} \eta_1=x_1 & \eta_2=x_3 & \cdots & \eta_5=x_9 \\ \dot{\eta}_1=x_2=\dot{x}_1 & \dot{\eta}_2=x_4=\dot{x}_3 & \cdots & \dot{\eta}_5=x_{10}=\dot{x}_9 \end{array} \tag{22}$$

This leads to the Kalman filter process model, represented in matrix form as

$$\dot{\underline{x}}=F_P\underline{x}+\underline{\Omega}(\underline{\theta}(t),F), \quad F_P\in R^{10x10} \tag{23}$$

However, as previously stated, the forcing vector of the right-hand side of Eqs. (21) and (23) is not known. This way, since our interest is to estimate the generalized coordinates as well as this vector, we include those terms in the estimation problem by augmenting the ordinary state-vector; in this sense, the approach here adopted is similar to estimate non-modeled generalized forces, a procedure for which [26] has coined the term *shaping filter*. Firstly, we consider the forcing vector as the output of a linear filter driven by zero-mean Gaussian white noise:

$$\begin{array}{l} \dot{\underline{x}}_f=G_f\underline{w}_f, \quad \underline{x}_f,\ \underline{w}_f\in R^5, \quad \underline{w}_f\sim N(0,Q) \\ \underline{\Omega}=H_f\underline{x}_f \end{array} \tag{24}$$

Eq. (24), in which G_f and H_f are identity matrices of order 5, exhibit respectively the state-space process and observation models for the unknown forcing vector $\underline{\Omega}(\theta(t),F)$. Next, those equations are used to augment the system and observation state-space models for the original generalized coordinates according to the following equation:

$$\left\{\begin{array}{c}\dot{\underline{x}}\\ \dot{\underline{x}}_f\end{array}\right\}=\left[\begin{array}{cc}F_P & G_PH_f\\ 0_{5x10} & 0_{5x5}\end{array}\right]\left\{\begin{array}{c}\underline{x}\\ \underline{x}_f\end{array}\right\}+\left[\begin{array}{c}0_{10x5}\\ G_f\end{array}\right]\underline{w}_f \Rightarrow \dot{\underline{X}}=A\underline{X}+B\underline{w}_f, \quad A\in R^{15x15}, \quad B\in R^{15x5}, \tag{25}$$

that provide the process state-space model in which both the generalized coordinates and the forcing terms constitute the state variables to be estimated. In view of Eqs. (23) and (24), it should be emphasized that process uncertainties, expressed by the random vector $\underline{w}_f$, affect only the unknown forcing terms. This is a feasible assumption, since the simplification introduced by modeling the true experimental riser as two-bar compliant mechanism according to [24] is capable of reproducing large displacements of an actual continuous beam, whose elastic line results from the solution of an elliptical differential equation.

The observation equation for the augmented model will be assembled taking into account that the only measurements available are angular displacements of the bars, obtained from images grabbed by a video camera. Those images, through a segmentation procedure, provide Cartesian coordinates of a set of markers that are used to generate the corresponding angles. Inherent errors in the image segmentation procedure are modeled as zero-mean Gaussian noise with covariance matrix R, resulting in the observation equation, as follows:

$$\begin{array}{l} \underline{Y}=\left[\begin{array}{cc}H_P & 0_{5x5}\end{array}\right]\underline{X}+\underline{v}\Rightarrow \underline{Y}=H\underline{X}+\underline{v}, \quad H_P\in R^{5x10}, \quad \underline{v}\in R^5, \quad \underline{v}\sim N(0,R), \\ H_P(i,j)=\left\{\begin{array}{ll}1 & \text{if} \quad i=k+1, \quad j=2k+1, \quad k=0,\ 1,\ 2,\ 3,\ 4\\ 0, & \text{otherwise}\end{array}\right. \end{array} \tag{26}$$

The state-space representation of the riser dynamical model according to Eqs. (25) and (26) is hybrid (continuous-discrete), since the state evolves continuously, whereas measurements are available at specific sample times. For computational purposes, in this work the continuous process model was discretized (with the aid of a built-in function in *Octave*) using the same time-step as that of the measurements, i.e., each kth iteration of the filter corresponds to a new measurement available. The obtained discrete-time process model is, then,

$$\underline{X}(t_k)=\Phi(t_k,t_{k-1})\underline{X}(t_{k-1})+B_d(t_k)\underline{w_f}(t_k), \tag{27}$$

in which $\underline{X}(t_k)$ is the state vector at the kth time-step $k\Delta t$, $\Phi(t_k,t_{k-1})$ is the discrete-time transition matrix, and $B_d(t_k)\underline{w_f}(t_k)$ is the discrete-time forcing vector. Accordingly, the discrete-time observation equation is

$$\underline{Y}(t_k)=H\underline{X}(t_k)+\underline{v}(t_k). \tag{28}$$

Regarding the estimation procedure, it suffices to mention that recursive estimation theory based on Kalman filtering is extensively discussed in the literature, see for instance [27]; thus, for the moment, we only state the hypotheses used and

provide a brief explanation of the algorithm through its equations. As already mentioned, white noise sequences $\underline{w}_f$ and $\underline{v}$ are assumed zero-mean Gaussian with associated covariance matrices; in addition, those sequences are considered mutually independent and, as a consequence of being Gaussian, they are also uncorrelated. Covariance matrices Q, for the state variables, and R, for the measurements, are admitted constant and diagonal.

For the model given by Eqs. (27) and (28), there is a forecast stage that seeks to produce the best estimates (in a stochastic least-squares sense) by propagating the previous estimated state based on the process model and its known (or admitted) statistics before new information is available. This way, Eq. (29)

$$\underline{X}^f(t_k) = \Phi \underline{X}^u(t_{k-1}) \tag{29}$$

provides the state estimation forecast and Eq. (30)

$$P^f(t_k) = P^u(t_{k-1}) + B_d Q(t_{k-1}) B_d^T \tag{30}$$

gives the estimation error covariance matrix forecast. When new data is available, an update stage provides proper correction to the forecasted estimates of the state and error covariance according to Eqs. (31) and (32),

$$\underline{X}^u(t_k) = \underline{X}^f(t_k) + K(t_k)\{\underline{y}(t_k) - H\underline{X}^f(t_k)\} \tag{31}$$

$$P^u(t_k) = (I - K(t_k)H)P^f(t_k) \tag{32}$$

it must be pointed out that in Eq. (31), $\underline{y}(t_k)$ is employed to represent the measurement vector, distinct from $\underline{Y}(t_k)$, measurement model.

The correction is provided by the Kalman gain matrix, computed according to Eq. (33)

$$K(t_k) = P^f(t_k)H\{HP^f(t_k)H^T + R(t_k)\}^{-1}, \tag{33}$$

thus completing the prediction–correction steps necessary for the next iteration of the filter.

4. Results and discussion

The previously described experimental setup grabs images at a rate of 28 frames/s, thus providing observations of the position of each one of the five markers attached to the suspended cable at every 0.036 s. Computed Cartesian coordinates of the markers were used to get the effective angular observations for the Kalman filter estimation procedure. The covariance matrices were $Q = 0.9I_{15}$ (process model noise covariance matrix, assumed constant), $R = 0.01I_5$ (measurement model noise covariance matrix, assumed constant) and $P_0 = 0.5I_{15}$ (state-estimation error covariance matrix); the initial state-vector was

$$[-0.0183;\ 0.0276;\ 0.0085;\ 0.0262;\ 0.0633;\ 0.253;\ -0.5087;\ 0.011;\ 0.245;\ -0.189;\ 0.0376;\ 0.025;\ 0.0153;\ 0.0063;\ 0.0]^T,$$

obtained as the mean value of measurements from the three first frames grabbed. The last 5 state-variables correspond to bending moments computed using a static estimate of the traction force on the cable, $F = 0.5$ N.

Estimates of the state-variables angular displacements and velocities are shown in Figs. 12 and 13. Those ten variables are the ones of the "original" dynamical system, i.e., without the augmentation that included forcing terms as state variables to be estimated. From Fig. 12, one realizes that the results are coherent, since angular displacements have higher amplitudes

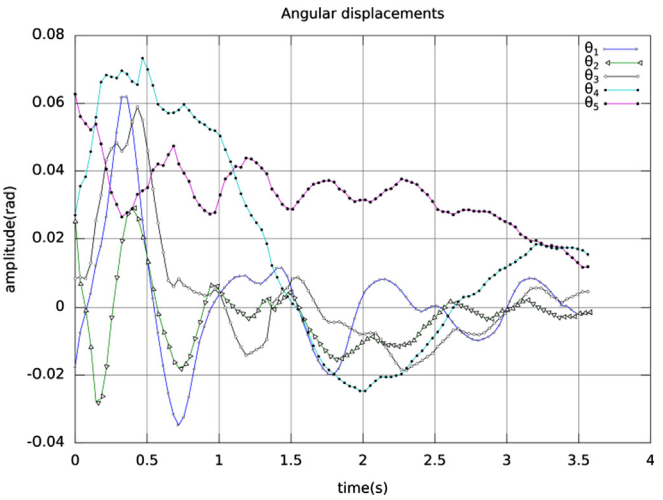

Fig. 12. Angular displacements of the model bars at the rotational springs.

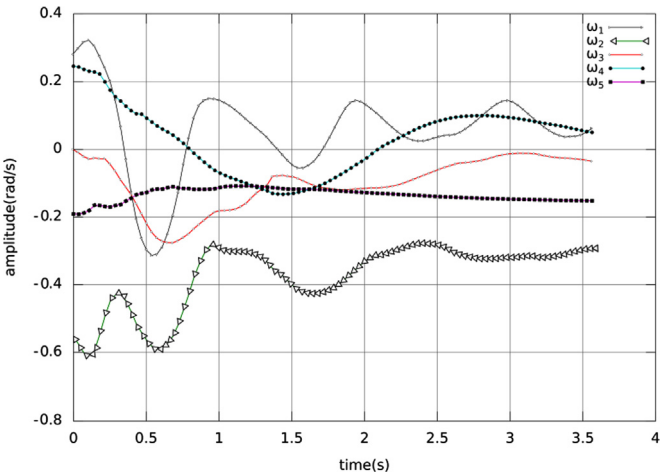

Fig. 13. Angular velocities of the model bars attached to rotational springs.

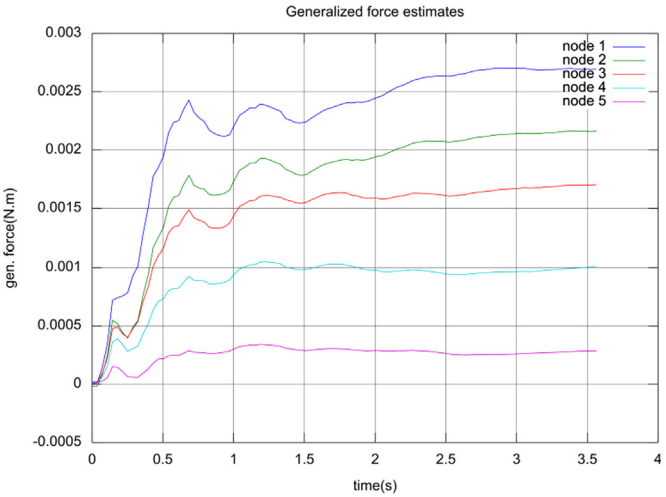

Fig. 14. Estimates of generalized forces.

for those nodes closer to the left-side of the cable; in addition, angular velocities behave accordingly, see Fig. 13. A possible source of questioning might be the reason why some of those state variables, namely ω_2, ω_3, ω_5, remain negative throughout the whole estimation procedure, an apparent incoherent result, since an alternating displacement is imposed at the fairlead point of the cable. This behavior can be explained taking into account that, according to the physical model described in Section 3.1, both angular displacements and velocities are represented in terms of consecutive relative coordinates.

Estimates of generalized forces are also in agreement with those theoretically expected. As it can be seen in Fig. 14, moments (in this case, generalized forces are bending moments each spring/bar setting) at the left-side of the cable present higher amplitudes, that decrease towards the right-side. It must be pointed out that the generalized force corresponding to state-variable number 15, the bending moment close to the free-end of the cable (node 5), stabilizes at 2.58×10^{-4} N m, about four times smaller than the one at its adjacent node.

The generalized forces, state-variables 11–14 (captions "node 1" to "node 4" on Fig. 15) of the augmented state-space model, are used to compute estimates of tension on the cable; the amplitudes of the 15th state-variable (caption "node 5" on Fig. 15) remain practically zero during the whole estimation process for the same reason stated in the previous paragraph, and are not considered in the computation of cable tension estimates. According to Fig. 15, the mean value thus calculated converges to 23.9 N at the end of the estimation process.

Quantitative evidence to support the convergence of the estimation procedure is provided by the behavior of the error covariance matrix and of the normalized estimation residual. The time-history of the Euclidean norm of the estimation error covariance matrix $P^u(t_k)$ is depicted in Fig. 16, from which it is possible to realize that, after positive gradients at the

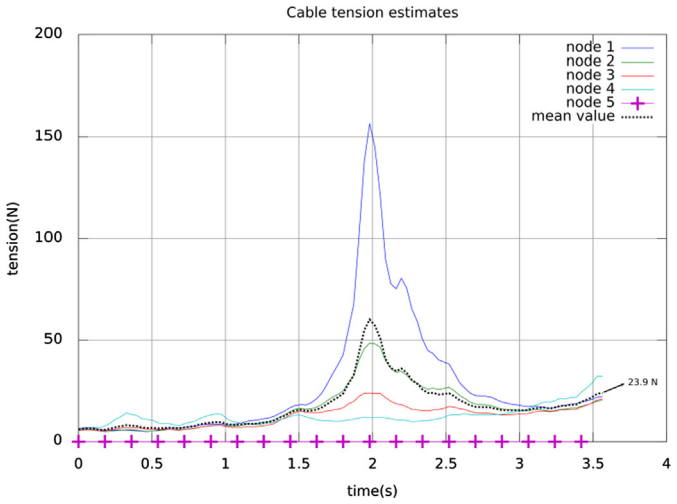

Fig. 15. Estimates of cable tension.

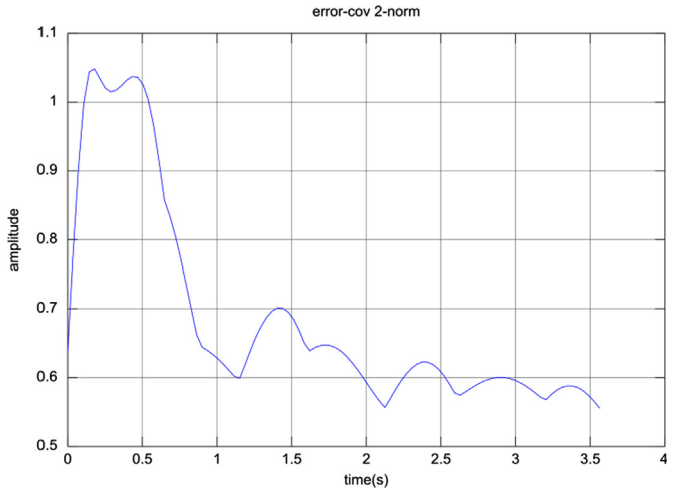

Fig. 16. Error covariance matrix Euclidean norm.

beginning of the process, as more observations are available, from $t \cong 0.5$ s, the error decreases towards a mean steady-state value, which indicates that the procedure has converged. This condition is, however, not enough to guarantee the actual convergence. As stated by [27], actual convergence of the estimation process must be asserted by the inspection of the difference between the effective measurement and its value as calculated by the filter using the last available state estimate. An estimation process is considered convergent once the normalized observation residuals, given by Eq. (34),

$$r_v = \frac{1}{\ell \sigma_\nu} \sum_{j=1}^{\ell} (\underline{y}_j(t_k) - \underline{X}_j^u(t_k)), \tag{34}$$

in which ℓ represents measurement vector dimension (in our case, $\ell = 5$), are zero-mean Gaussian with standard deviation between $-3\sigma_\nu$ and $3\sigma_\nu$. In Fig. 17, it is shown that those requirements are fulfilled because, since $E[r_v] = 0.0267$ and $E[r_v^2] = 0.0165$. However, one could raise an issue about the mean-value as valid convergence criterion, for there is a constant bias between approximately 1.5 and 3.3 s on the simulation. In reply to this questioning, Fig. 18 presents a comparison among the time-evolution of the state-variables θ_1–θ_5 in simulations using the shaping-filter proposed approach ("s–f estimates") and only according to the phenomenological model("model-only"), for the same input condition. It may be observed that the model-only outcomes present higher amplitudes than the ones provided by the filter estimates, thus corroborating the asserted convergence.

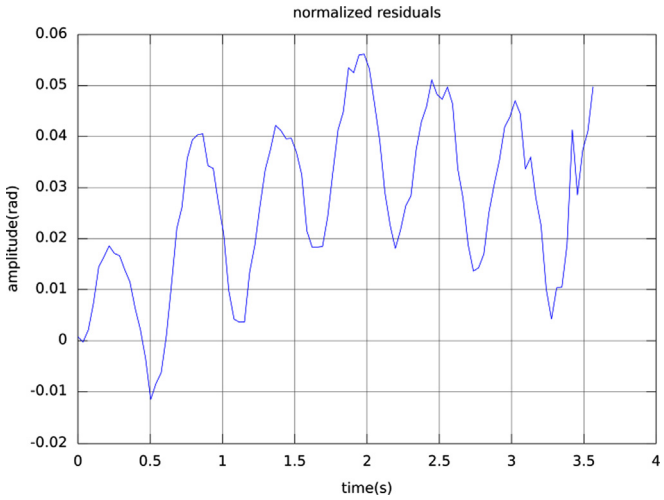

Fig. 17. Normalized observation residuals.

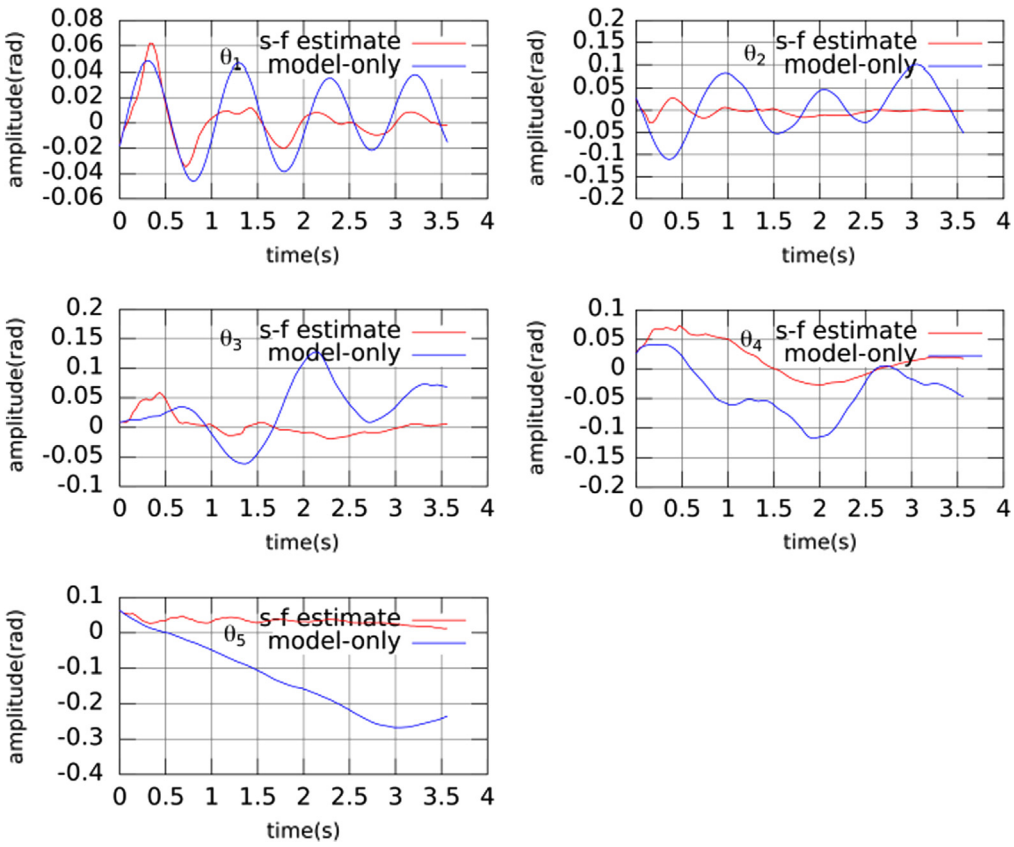

Fig. 18. Time evolution of the state-variables (modeled and estimated).

5. Conclusions

This work investigated the use of a new approach to analyze the dynamics of an underwater suspended cable through image-based instrumentation associated to parameter estimation techniques. A scaled-model riser has undertaken several tests in a controlled environment. Simple self calibration procedures applied to images grabbed by a video camera provided observations used in a state-space model of the system dynamics obtained from the application of compliant mechanisms theory to spatially discretize the riser specimen. The system dynamical model was simulated through a non-linear Kalman

filter in which the state-variables of the augmented state-space vector included the unknown generalized forces at the end of each discretized segment of the cable. Results from the simulations suggest that it is possible to use the described approach to estimate both the bending moments along the cable and the tension force at its free end. This assertion is corroborated by statistical evidence of the convergence of the filtering process, namely, decreasing error covariance matrix Euclidean norm and consistency of the normalized observation residuals.

Further work is under way to include new experimental results and to incorporate damping on the process model, based on results from finite element analysis, or compliant mechanisms discretization and operational modal analysis of the suspended cable. Those new experimental data will also allow one to obtain more accurate process noise matrices, since the motion of each segment in the simplified model represents the contribution of several vibration modes.

Acknowledgments

This work was supported by Brazilian National Council of Science and Technology (CNPq) as part of the Project 471880/2006-0 – 'Identification of Kinematics of Ships and Offshore Structures Using Computer Vision'. Third author also gratefully acknowledges CNPq for financial support.

Appendix A

The following equations were obtained through proper application of Eqs. (9)–(12)) for the five generalized coordinates $(\theta_1, \ldots, \theta_5)$ describing the configuration of the discretized scaled-model riser:

$$\begin{aligned}
&\frac{d}{dt}\left(\frac{\partial L}{\partial \dot{\theta}_1}\right)+\left(\frac{\partial L}{\partial \theta_1}\right)=F_{\theta 1} \Rightarrow \left[m\ell^2\left(\frac{\gamma^2}{4}+4\right)+5J\right]\ddot{\theta}_1+\left[\frac{m\ell^2}{2}(6+\gamma)\cos\,\theta_2+4J\right]\ddot{\theta}_2+\left[\frac{m\ell^2}{2}(4+\gamma)\cos(\theta_2+\theta_3)+3J\right]\ddot{\theta}_3\\
&+\left[\frac{m\ell^2}{2}(2+\gamma)\cos(\theta_2+\theta_3+\theta_4)+2J\right]\ddot{\theta}_4+\left[\frac{m\ell^2}{2}\gamma\,\cos(\theta_2+\theta_3+\theta_4+\theta_5)+3J\right]\ddot{\theta}_5\\
&-\frac{m\ell^2}{2}\left[(6+\gamma)\sin\,\theta_2\dot{\theta}_2^2+(4+\gamma)\sin(\theta_2+\theta_3)\dot{\theta}_2\dot{\theta}_3+(2+\gamma)\sin(\theta_2+\theta_3+\theta_4)\dot{\theta}_2\dot{\theta}_4+\gamma\,\sin(\theta_2+\theta_3+\theta_4+\theta_5)\dot{\theta}_2\dot{\theta}_5\right]\\
&-\frac{m\ell^2}{2}\left[(4+\gamma)\sin(\theta_2+\theta_3)\dot{\theta}_3^2+(2+\gamma)\sin(\theta_2+\theta_3+\theta_4)\dot{\theta}_3\dot{\theta}_4+\gamma\,\sin(\theta_2+\theta_3+\theta_4+\theta_5)\dot{\theta}_3\dot{\theta}_5\right]\\
&-\frac{m\ell^2}{2}\left[(2+\gamma)\sin(\theta_2+\theta_3+\theta_4)\dot{\theta}_4^2+\gamma\,\sin(\theta_2+\theta_3+\theta_4+\theta_5)\dot{\theta}_4\dot{\theta}_5\right]-\frac{m\ell^2}{2}\left[\gamma\,\sin(\theta_2+\theta_3+\theta_4+\theta_5)\dot{\theta}_5^2\right]+k_1\theta_1\\
&+p_s\ell^2\left[\left(\frac{\gamma}{2}+4\right)\cos\,\theta_1+\left(\frac{\gamma}{2}+3\right)\cos(\theta_1+\theta_2)+\left(\frac{\gamma}{2}+2\right)\cos(\theta_1+\theta_2+\theta_3)+\left(\frac{\gamma}{2}+1\right)\cos(\theta_1+\theta_2+\theta_3+\theta_4)\right]\\
&+p_s\ell^2\left[\frac{\gamma}{2}\cos(\theta_1+\theta_2+\theta_3+\theta_4+\theta_5)\right]=-F\ell[\,\sin\,\theta_1+\,\sin(\theta_1+\theta_2)+\,\sin(\theta_1+\theta_2+\theta_3)]\,\cos(\theta_1+\theta_2+\theta_3+\theta_4+\theta_5)\\
&-F\ell[\,\sin(\theta_1+\theta_2+\theta_3+\theta_4)+\,\sin(\theta_1+\theta_2+\theta_3+\theta_4+\theta_5)]\,\cos(\theta_1+\theta_2+\theta_3+\theta_4+\theta_5)\\
&+F\ell[\,\cos\,\theta_1+\,\cos(\theta_1+\theta_2)+\,\cos(\theta_1+\theta_2+\theta_3)]\,\sin(\theta_1+\theta_2+\theta_3+\theta_4+\theta_5)\\
&+F\ell[\,\cos(\theta_1+\theta_2+\theta_3+\theta_4)+\,\cos(\theta_1+\theta_2+\theta_3+\theta_4+\theta_5)]\,\sin(\theta_1+\theta_2+\theta_3+\theta_4+\theta_5) \qquad (A-1)
\end{aligned}$$

$$\begin{aligned}
&\frac{d}{dt}\left(\frac{\partial L}{\partial \dot{\theta}_2}\right)-\frac{\partial L}{\partial \theta_2}=F_{\theta 2} \Rightarrow \left[\frac{m\ell^2}{2}(6+\gamma)\cos\,\theta_2+4J\right]\ddot{\theta}_1+\left[\frac{m\ell^2}{2}\left(\frac{\gamma^2}{2}+6\right)+4J\right]\ddot{\theta}_2+\left[\frac{m\ell^2}{2}(4+\gamma)\cos\,\theta_3+3J\right]\ddot{\theta}_3\\
&+\left[\frac{m\ell^2}{2}(2+\gamma)\cos(\theta_3+\theta_4)+2J\right]\ddot{\theta}_4+\left[\frac{m\ell^2}{2}\gamma\,\cos(\theta_3+\theta_4+\theta_5)+J\right]\ddot{\theta}_5\\
&-\frac{m\ell^2}{2}\left[(6+\gamma)\sin\,\theta_2\dot{\theta}_1\dot{\theta}_2+(4+\gamma)\sin\,\theta_3\dot{\theta}_3^2+(2+\gamma)\sin(\theta_3+\theta_4)\dot{\theta}_3\dot{\theta}_4+\gamma\,\sin(\theta_3+\theta_4+\theta_5)\dot{\theta}_3\dot{\theta}_5\right]\\
&+\frac{m\ell^2}{2}\left[(2+\gamma)\sin(\theta_3+\theta_4)\dot{\theta}_4^2+\gamma\,\sin(\theta_3+\theta_4+\theta_5)\dot{\theta}_5^2\right]\\
&+\frac{m\ell^2}{2}[(6+\gamma)\sin\,\theta_2\dot{\theta}_1\dot{\theta}_2+(4+\gamma)\sin(\theta_2+\theta_3)\dot{\theta}_1\dot{\theta}_3+(2+\gamma)\sin(\theta_2+\theta_3+\theta_4)\dot{\theta}_1\dot{\theta}_4+\gamma\,\sin(\theta_2+\theta_3+\theta_4+\theta_5)\dot{\theta}_1\dot{\theta}_5]\\
&+k_2\theta_2+p_s\ell^2\left[\left(\frac{\gamma}{2}+3\right)\cos(\theta_1+\theta_2)+\left(\frac{\gamma}{2}+2\right)\cos(\theta_1+\theta_2+\theta_3)+\left(\frac{\gamma}{2}+1\right)\cos(\theta_1+\theta_2+\theta_3+\theta_4)\right]\\
&+p_s\ell^2\left[\frac{\gamma}{2}\cos(\theta_1+\theta_2+\theta_3+\theta_4+\theta_5)\right]=\\
&-F\ell[\,\sin(\theta_1+\theta_2)+\,\sin(\theta_1+\theta_2+\theta_3)+\,\sin(\theta_1+\theta_2+\theta_3+\theta_4)\\
&+\,\sin(\theta_1+\theta_2+\theta_3+\theta_4+\theta_5)]\,\cos(\theta_1+\theta_2+\theta_3+\theta_4+\theta_5)\\
&+F\ell[\,\cos(\theta_1+\theta_2)+\,\cos(\theta_1+\theta_2+\theta_3)+\,\cos(\theta_1+\theta_2+\theta_3+\theta_4)\\
&+\,\cos(\theta_1+\theta_2+\theta_3+\theta_4+\theta_5)]\,\sin(\theta_1+\theta_2+\theta_3+\theta_4+\theta_5) \qquad (A-2)
\end{aligned}$$

$$\frac{d}{dt}\left(\frac{\partial L}{\partial \dot{\theta}_3}\right)-\frac{\partial L}{\partial \theta_3}=F_{\theta 3}\Rightarrow \left[\frac{m\ell^2}{2}(4+\gamma)\cos(\theta_2+\theta_3)+3J\right]\ddot{\theta}_1+\left[\frac{m\ell^2}{2}(4+\gamma)\cos\ \theta_3+3J\right]\ddot{\theta}_2+\left[\frac{m\ell^2}{2}\left(\frac{\gamma^2}{2}+4\right)+3J\right]\ddot{\theta}_3$$
$$+\left[\frac{m\ell^2}{2}(2+\gamma)\cos\ \theta_4+2J\right]\ddot{\theta}_4+\left[\frac{m\ell^2}{2}\gamma\ \cos(\theta_4+\theta_5)+J\right]\ddot{\theta}_5$$
$$-\frac{m\ell^2}{2}\left[(4+\gamma)\sin(\theta_2+\theta_3)\dot{\theta}_1\dot{\theta}_2+(4+\gamma)\sin(\theta_2+\theta_3)\dot{\theta}_1\dot{\theta}_3+(4+\gamma)\sin\ \theta_3\dot{\theta}_2\dot{\theta}_3+(2+\gamma)\sin\ \theta_4\dot{\theta}_4^2\right]$$
$$+\frac{m\ell^2}{2}\left[\gamma\ \sin(\theta_4+\theta_5)\dot{\theta}_4\dot{\theta}_5+\gamma\ \sin(\theta_4+\theta_5)\dot{\theta}_5^2\right]+k_2\theta_3$$
$$+p_s\ell^2\left[\left(\frac{\gamma}{2}+2\right)\cos(\theta_1+\theta_2+\theta_3)+\left(\frac{\gamma}{2}+1\right)\cos(\theta_1+\theta_2+\theta_3+\theta_4)+\frac{\gamma}{2}\cos(\theta_1+\theta_2+\theta_3+\theta_4+\theta_5)\right]=$$
$$-F\ell[\ \sin(\theta_1+\theta_2+\boldsymbol{\theta_3})+\ \sin(\theta_1+\theta_2+\boldsymbol{\theta_3}+\theta_4)+\ \sin(\theta_1+\theta_2+\boldsymbol{\theta_3}+\theta_4+\theta_5)]\cos(\theta_1+\theta_2+\boldsymbol{\theta_3}+\theta_4+\theta_5)$$
$$+F\ell[\ \cos(\theta_1+\theta_2+\boldsymbol{\theta_3})+\ \cos(\theta_1+\theta_2+\boldsymbol{\theta_3}+\theta_4)$$
$$+\ \cos(\theta_1+\theta_2+\boldsymbol{\theta_3}+\theta_4+\theta_5)]\sin(\theta_1+\theta_2+\boldsymbol{\theta_3}+\theta_4+\theta_5) \qquad (A-3)$$

$$\frac{d}{dt}\left(\frac{\partial L}{\partial \dot{\theta}_4}\right)-\frac{\partial L}{\partial \theta_4}=F_{\theta 4}\Rightarrow \left[\frac{m\ell^2}{2}(2+\gamma)\cos(\theta_2+\theta_3+\theta_4)+2J\right]\ddot{\theta}_1$$
$$+\left[\frac{m\ell^2}{2}(2+\gamma)\cos(\theta_3+\theta_4)+2J\right]\ddot{\theta}_2+\left[\frac{m\ell^2}{2}(2+\gamma)\cos\ \theta_4+2J\right]\ddot{\theta}_3$$
$$+\left[\frac{m\ell^2}{2}\left(\frac{\gamma^2}{2}+2\right)+2J\right]\ddot{\theta}_4+\left[\frac{m\ell^2}{2}\gamma\ \cos\ \theta_5+J\right]\ddot{\theta}_5$$
$$-\frac{m\ell^2}{2}\left[(2+\gamma)\sin(\theta_2+\theta_3+\theta_4)\dot{\theta}_1\dot{\theta}_2+(2+\gamma)\sin(\theta_2+\theta_3+\theta_4)\dot{\theta}_1\dot{\theta}_3\right.$$
$$\left.+(2+\gamma)\sin(\theta_2+\theta_3+\theta_4)\dot{\theta}_1\dot{\theta}_4+(2+\gamma)\sin(\theta_3+\theta_4)\dot{\theta}_2\dot{\theta}_3\right]$$
$$+\frac{m\ell^2}{2}\left[(2+\gamma)\sin(\theta_3+\theta_4)\dot{\theta}_2\dot{\theta}_4+(2+\gamma)\sin(\theta_3+\theta_4)\dot{\theta}_2\dot{\theta}_4\gamma\ \sin\ \theta_4\dot{\theta}_3\dot{\theta}_4+\gamma\ \sin\ \theta_5\dot{\theta}_5^2\right]+k_2\theta_4$$
$$+p_s\ell^2\left[\left(\frac{\gamma}{2}+1\right)\cos(\theta_1+\theta_2+\theta_3+\theta_4)+\frac{\gamma}{2}\cos(\theta_1+\theta_2+\theta_3+\theta_4+\theta_5)\right]=$$
$$-F\ell[\ \sin(\theta_1+\theta_2+\boldsymbol{\theta_3}+\theta_4)+\ \sin(\theta_1+\theta_2+\boldsymbol{\theta_3}+\theta_4+\theta_5)]\cos(\theta_1+\theta_2+\boldsymbol{\theta_3}+\theta_4+\theta_5)$$
$$+F\ell[\ \cos(\theta_1+\theta_2+\boldsymbol{\theta_3}+\theta_4)+\ \cos(\theta_1+\theta_2+\boldsymbol{\theta_3}+\theta_4+\theta_5)]\sin(\theta_1+\theta_2+\boldsymbol{\theta_3}+\theta_4+\theta_5) \qquad (A-4)$$

$$\frac{d}{dt}\left(\frac{\partial L}{\partial \dot{\theta}_5}\right)-\frac{\partial L}{\partial \theta_5}=F_{\theta 5}\Rightarrow \left[\frac{m\ell^2}{2}\gamma\ \cos(\theta_2+\theta_3+\theta_4+\theta_5)+J\right]\ddot{\theta}_1+\left[\frac{m\ell^2}{2}\gamma\ \cos(\theta_3+\theta_4+\theta_5)+J\right]\ddot{\theta}_2$$
$$+\left[\frac{m\ell^2}{2}\gamma\ \cos(\theta_4+\theta_5)+J\right]\ddot{\theta}_3+\left[\frac{m\ell^2}{2}\gamma\ \cos(\theta_4+\theta_5)+J\right]\ddot{\theta}_4+\left[\frac{m\ell^2\gamma}{2\ 2}+J\right]\ddot{\theta}_5$$
$$-\frac{m\ell^2}{2}\left[\gamma\ \sin(\theta_2+\theta_3+\theta_4+\theta_5)(\dot{\theta}_1\dot{\theta}_2+\dot{\theta}_1\dot{\theta}_3+\dot{\theta}_1\dot{\theta}_4+\dot{\theta}_1\dot{\theta}_5)+\gamma\ \sin(\theta_3+\theta_4+\theta_5)(\dot{\theta}_2\dot{\theta}_3+\dot{\theta}_2\dot{\theta}_4+\dot{\theta}_2\dot{\theta}_5)\right]$$
$$+\frac{m\ell^2}{2}\left[\gamma\ \sin(\theta_4+\theta_5)(\dot{\theta}_3\dot{\theta}_4+\dot{\theta}_3\dot{\theta}_5)+\gamma\ \sin\ \theta_5\dot{\theta}_4\right]$$
$$+\frac{m\ell^2}{2}\left[\gamma\ \sin(\theta_2+\theta_3+\theta_4+\theta_5)\dot{\theta}_1\dot{\theta}_5+\gamma\ \sin(\theta_3+\theta_4+\theta_5)\dot{\theta}_2\dot{\theta}_5+\gamma\ \sin(\theta_4+\theta_5)\dot{\theta}_3\dot{\theta}_5+\gamma\ \sin\ \theta_5\dot{\theta}_4\dot{\theta}_5\right]+k_2\theta_5$$
$$+p_s\ell^2\left[\frac{\gamma}{2}\cos(\theta_1+\theta_2+\theta_3+\theta_4+\theta_5)\right]=0 \qquad (A-5)$$

References

[1] T.B. Moeslund, A. Hilton, V. Krüger, A survey of advances on vision-based human motion capture and analysis, Comput. Vision Image Understanding 104 (2006) 90–96.
[2] M. Shortis, E. Harvey, D. Abdo, A review of underwater stereo image measurement for marine biology and ecology applications, Oceanogr. Mar. Biol.: Annu. Rev. 47 (2009) 257–292.
[3] R.J. Schalkoff, Digital Image Processing and Computer Vision, John Wiley and Sons, New York, 1989.
[4] R.I. Hartley, Self-calibration of stationary cameras, Int. J. Comput. Vision 22 (1) (1997) 5–23.
[5] A. Valdés, J.I. Ronda, Camera autocalibration and the calibration pencil, J. Math. Imaging Vision 23 (2005) 167–174.
[6] A. Habed, B. Boufama, Camera self-calibration from bivariate polynomial equations and coplanarity constraints, Image Vision Comput. 24 (2006) 498–514.
[7] J.F. Menudet, J.M. Becker, T. Fournel, C. Menessier, Plane-based camera self-calibration by metric rectification of images, Image Vision Comput. 26 (7) (2007) 1–22.
[8] O. Faugeras, Three Dimensional Computer Vision: A Geometrical Viewpoint, The MIT Press, Cambridge, USA, 1993.
[9] F. Ayres Jr, Theory and Problems of Projective Geometry, Schaum Publishing Co, New York, 1967.
[10] H. Beghin, Mécanique Théorique et Appliquée, Tome 1. Gauthier-Villars, Paris, 1952.

[11] J. Pérès, Mécanique Générale, Masson & Cie, Paris, 1962.
[12] C.P. Pesce, Mecânica de cabos e tubos submersos lançados em catenária: uma abordagem analítica e experimental, Escola Politécnica, Universidade de São Paulo, 1997 (Tese de livre-docência).
[13] L.A. Campos, Análise de esforços dinâmicos na região do 'touchdown point' de um riser rígido em catenária, Escola Politécnica, Universidade de São Paulo, 1997 (MSc thesis).
[14] F.C.M. Takafuji, Dinâmica tridimensional de risers, Escola Politécnica, Universidade de São Paulo, 2010 (Ph.D. thesis).
[15] A. Bando., K. Otsuka, Y. Ikeda, Experimental study of an 8-shaped oscillating flexible riser, in: Proceedings of the Twelfth (2002) International Offshore and Polar Engineering Conference, Kitakiushu, Japan, 2002, pp. 510–514.
[16] L.F. Menezes Jr, Processamento de imagens na análise dinâmica de risers de produção de petróleo com modelo de escala reduzida em ambiente de laboratório, Tese de doutorado, Faculdade de Engenharia Mecânica, Unicamp, 2008.
[17] R.M. Amarante, Estudo da estática e dinâmica de linhas, sob configuração de catenária, através da identificação geométrica, processamento e análise de imagens digitais, MSc Thesis, Escola Politécnica, Universidade de São Paulo, 2010.
[18] D.L.B.R. Jurjo, C. Magluta, N. Roitman, P.B. Gonçalves, Experimental methodology for the dynamic analysis of slender structures based on digital image processing, Mech. Syst. Signal Process. 24 (2010) 1369–1382.
[19] Z. Liu, D. Krys, The use of laser range finder on a robotic platform for pipe inspection, Mech. Syst. Signal Process. 31 (2012) 246–257.
[20] N. Otsu, A threshold selection method from gray-level histograms, IEEE Trans. Syst. Man Cybern. v.SMC-9 (1) (1979) 62–66.
[21] J. Serra, Image Analysis and Mathematical Morphology, vol. 1, Academic Press, London, 1989.
[22] L. Vincent, Efficient computation of various types of skeletons, Proceedings of the SPIE, Medical Image V 1445 (1991) 297–311.
[23] B.K.P. Horn, Robot Vision, The MIT Press, Cambridge, Massachusetts, 1986.
[24] L.L. Howell, Compliant Mechanisms, Wiley Interscience, New York, USA, 2001.
[25] B.L. Weight, Development and design of constant-force mechanisms, Brigham Young University, Department of Mechanical Engineering, 2001 (thesis).
[26] P.S. Maybeck, Stochastic Models, Estimation and Control, vol. 1, Academic Press, New York, 1979.
[27] A.H. Jazwinksi, Stochastic Processes and Filtering Theory, Academic Press, New York, 1970.